Optics Letters

Thermally tunable and efficient second-harmonic generation on thin-film lithium niobate with integrated micro-heater

Xiaoyue Liu,[1,3] Chi Zhang,[2] Ying Pan,[1] Rui Ma,[1] Xian Zhang,[1] Mengwen Chen,[2] Lin Liu,[1] Zhenda Xie,[2] Shining Zhu,[2] Siyuan Yu,[1] and Xinlun Cai[1,*]

[1]State Key Laboratory of Optoelectronic Materials and Technologies, School of Electronics and Information Technology, Sun Yat-sen University, Guangzhou 510275, China
[2]National Laboratory of Solid State Microstructures, College of Engineering and Applied Sciences, College of Electronic Science and Engineering, and School of Physics, Nanjing University, Nanjing 210093, China
[3]e-mail: liuxy335@mail2.sysu.edu.cn
*Corresponding author: caixlun5@mail.sysu.edu.cn

Received 19 July 2022; revised 25 August 2022; accepted 25 August 2022; posted 29 August 2022; published 16 September 2022

In this Letter, we report thermo-optic tunable and efficient second-harmonic generation (SHG) based on an X-cut periodically poled lithium niobate (PPLN) waveguide. By applying an on-chip heater with thermo-isolation trenches and combining a type-0 quasi-phase matching mechanism, we experimentally achieve a high on-chip SHG conversion efficiency of 2500–3000% W^{-1} cm^{-2} and a large tuning power efficiency of 94 pm/mW inside a single 5-mm-long straight PPLN waveguide. Our design is for energy-efficient, high-performance nonlinear applications, such as wavelength conversion, highly tunable coherent light sources, and photon-pair generation.

https://doi.org/10.1364/OL.470867

Efficient second-order nonlinear ($\chi^{(2)}$) processes [1]—including second-harmonic generation (SHG), sum/difference-frequency generation (SFG/DFG), and optical parametric oscillators—have numerous applications, such as entangled photon-pair sources [2,3], coherent light generation [4], and optical parametric amplifiers [5–7]. Among them are highly tunable coherent light sources—with SHG a prominent example—playing a crucial role in optical communications [8], spectroscopy [9], frequency metrology [10], and sensing [11]. This highlights the desire to achieve a high conversion efficiency and large tunability in the SHG process.

Lithium niobate—benefiting from its large $\chi^{(2)}$ tensor ($d_{33} \sim 27$ pm/V), high refractive index (~2.2), and low-loss optical window (from 0.35 μm to 5.2 μm) [12]—is a superior material of choice for nonlinear optical applications. The ferroelectric property [13] of lithium niobate allows periodic inversion of the optical crystal domains to achieve type-0 quasi-phase-matching (QPM) between fundamental spatial modes. This technique takes advantage of the largest nonlinear coefficient d_{33} as well as the large mode overlap, which is crucial for achieving a high conversion efficiency.

Recently, thin-film lithium niobate (TFLN) [14] has emerged as a versatile nanophotonic platform. With the advantages of high optical confinement, enhanced light–matter interaction, and flexible dispersion control, TFLN-based PPLN devices offer significant improvement to the nonlinear conversion efficiency compared to their legacy PPLN counterparts [15–19]. However, with the large index contrast of TFLN waveguides (~0.7), the phase-matching condition is very sensitive to waveguide dimension variation, which places stringent requirements on the accuracy of the device parameters of the TFLN-based PPLN waveguide, such as poling period and waveguide dimensions [20]. Indeed, the random variation of the TFLN thickness and unavoidable fabrication imperfections strongly affect the device performance, especially the central wavelength of the SHG.

To address this issue, a TFLN-based PPLN device capable of actively tuning the central wavelength of SHG is highly desirable. In legacy SHG devices, the central wavelength can be tuned by changing the substrate temperature by using a thermoelectric cooler (TEC) [21–23]. Based on a TEC-tuning scheme, a tuning efficiency of ~1.06 nm/K [22] and −1.71 nm/K [23] were achieved on a type-I unpoled waveguide and a dispersion-engineered Z-cut type-0 PPLN waveguide, respectively. However, the former was obtained by exploiting the strong thermal birefringence of lithium niobate, but at the expense of conversion efficiency because of the weak mode overlap. The latter imposed stringent requirements on the waveguide size required by delicate group-velocity matching, thus reducing the design freedom of the functional device. Crucially, TEC-based solutions suffer from bulky and power-consuming issues [24].

In this study, we experimentally demonstrate a method to achieve tunable and efficient SHG based on an X-cut TFLN platform by using an on-chip microheater and air trenches for thermal isolation. Our design avoids heating up the entire chip by generating a highly localized temperature field distribution, which significantly reduces the heating power (~mW) and makes it scalable to architecture comprising multiple tunable devices, including but not limited to tunable nonlinear waveguides. In our study, we achieved a wavelength tuning range of approximately 5 nm at a telecom band of only 50 mW, corresponding to a large thermal-tuning efficiency of 94 pm/mW. Also, we achieved a

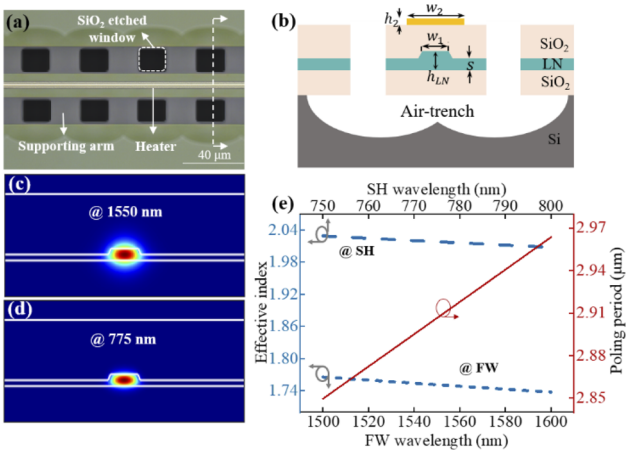

Fig. 1. (a) Microscopy image of the fabricated thermal-isolated device. (b) Schematic cross section of the tunable PPLN waveguide. The electrical field profiles of TE_{00} mode (c) at 1550 nm and (d) at 775 nm. (e) Simulated effective index of TE_{00} mode at FW and SH, and calculated poling period curves as a function of wavelength.

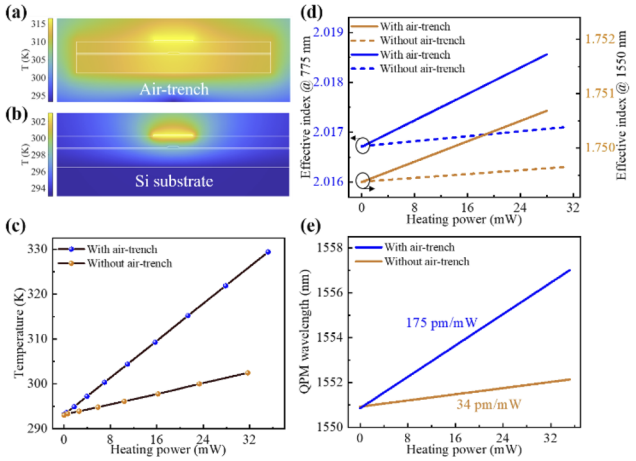

Fig. 2. Simulated temperature distribution of the (a) thermal-isolated device and (b) isolation-free device with the heating power of 18 mW. (c) Simulated temperature of the heated waveguide as a function of heating power. (d) Calculated TE_{00} mode index at 775 nm (blue lines) and 1550 nm (orange lines) and the corresponding QPM wavelength of the thermal-isolated device (solid lines) and the isolation-free device (dot lines) as a function of heating power. (e) Simulated QPM wavelength as a function of heating power for poling period of 2.9 μm.

type-0 QPM process with a high SHG normalized efficiency of 2500–3000% W^{-1} cm^{-2} during thermo-optic tuning.

Figure 1(a) shows a microscopy image of the fabricated device, based on an X-cut TFLN wafer (NANOLN Inc.) with a 360-nm-thick LN thin film and a 2.5-μm buried oxide layer on a silicon substrate. Figure 1(b) shows the schematic of the device. The rib height and top width of the designed PPLN waveguide were 180 nm and 800 nm, respectively. As shown in Figs. 1(c) and 1(d), we chose the polarization of the fundamental wave (FW) and second harmonic (SH) to be TE_{00}, corresponding to a type-0 QPM mechanism. By simulating their effective indices by using the finite-element method (FEM), we designed the poling period to be $\Lambda = \frac{\lambda_1}{2(n_2-n_1)}$ [in Fig. 1(e)], in which n_1 and n_2 are the effective indices of the TE_{00} mode at FW (λ_1) and SH (λ_2), respectively. Considering that the fabrication error in the waveguide geometry results in a deviation between the predicted and measured phase-matching wavelength, we experimentally prepared several PPLN waveguides with poling periods ranging from 2.87 to 2.93 μm in 10-nm steps.

We tuned these PPLN devices thermally by heating the microheaters with air trenches. The microheater was composed of a nichrome (NiCr) electrode with a thickness and width of 200 nm and 5 μm, respectively. It was located on top of the PPLN waveguide, separated by an upper-cladding layer with a thickness of 1.5 μm that is large enough to minimize the metal absorption loss. The current through the high-resistance metal heater induced Joule heating, which was gradually transferred to the TFLN devices. This changed the refractive index of the LN waveguide because of the thermo-optic effect and further shifted the phase-matched wavelength by affecting the QPM condition. Importantly, the integration of air trenches around and underneath the waveguide can significantly prevent heat leakage in the vertical and lateral directions because of the low heat conductivity of air [~0.026 W/(m K)].

We simulated two devices with and without air trenches to study the thermal-isolation effect of air trenches. First, we performed an electrothermal analysis by using a Multiphysics model that included an electric current module in combination with a heat transfer module. Figures 2(c) and 2(d) show the temperature field distributions of the two devices under the same power level (~18 mW). Notice that the temperature of the device with an air trench (~315 K) is much higher than that of the device without an air trench (~298 K). Figure 2(e) shows the temperature of the waveguide as a function of the heating power. The simulated thermal tuning efficiency of the device with air-trenches is 1.35 K/mW—almost 5-times larger than that achieved in the isolation-free structure (~0.29 K/mW).

We further studied the thermo-optic (TO) tuning efficiency of the phase-matched wavelength. The TO coefficients of TE-polarized lights at FW and SH are given by the following [25]:

$$\left(\frac{dN_1}{dT}\right) = -2.6 + 19.8 \times 10^{-3}\, T(10^{-5}\ \mathrm{K}^{-1}),$$

$$\left(\frac{dN_2}{dT}\right) = -2.6 + 22.4 \times 10^{-3}\, T(10^{-5}\ \mathrm{K}^{-1}).$$

These equations apply to the temperature range of 300–515 K. We obtained the effective TE_{00}-mode indexes at both wavelengths under different heating powers. As shown in Fig. 2(d), the TE_{00}-mode indices depended linearly on the heating power. The slopes of the device with the air trench were >5-fold larger than those achieved in the isolation-free structure at both wavelengths. Because the effective refractive index curve of FW exhibits a steeper slope than that of SH, the phase-matched wavelength is red-shifted as the temperature increases. [22,26] We obtained the QPM wavelength under different heating powers with a constant poling period of 2.9 μm, according to the QPM condition:

$$\frac{2 \cdot [(n_2 - n_1) + (\Delta n_2 - \Delta n_1)]}{\lambda_1} = \frac{1}{\Lambda}.$$

In this equation, Δn is the difference in the effective refractive index of the TE_{00} mode with and without the heating power. As shown in Fig. 2(e), the device with the air trench exhibits

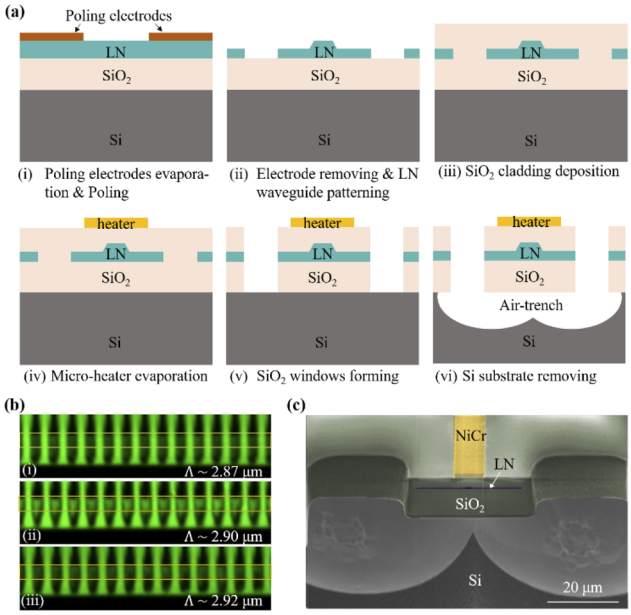

Fig. 3. (a) Fabrication flow of the device. (b) Period domains of devices with poling period of (i) 2.87 μm, (ii) 2.9 μm, and (iii) 2.92 μm, which are observed by SH confocal microscopy. The yellow boxes represent the area used to define the waveguide. (c) Scanning electron microscopy (SEM) image of the cross sectional view of the fabricated device.

a tuning efficiency of 175 pm/mW, whereas that of the device without the air trench is 34 pm/mW.

We fabricated thermally isolated TO PPLN waveguides by using the procedure depicted in Fig. 3(a). First, we evaporated comb-shaped poling electrodes, including 30-nm NiCr and 40-nm Au, on top of the TFLN [step (i)]. The gap between the in-plane positive and negative electrodes was 6 μm. By applying high-voltage pulses to the patterned electrodes, we formed a ferroelectric domain structure and checked it by confocal microscopy [15]. Figure 3(b) shows the period domains of several devices with poling periods of 2.87, 2.9, and 2.92 μm.

After poling, we completely removed the electrodes and fabricated the ridge PPLN waveguides by using electron beam lithography (EBL) and inductively coupled plasma (ICP) etching [step (ii)]. Then, we deposited a cladding layer of 1.5-μm silicon oxide on the chip via plasma-enhanced chemical vapor deposition (PECVD) [step (iii)]. Next, we formed NiCr heaters on the top of the PPLN waveguide [step (iv)], with EBL, electron beam evaporation (EBE), and lift-off processes. Finally, we removed SiO_2 windows on both sides of the waveguide and the underlying silicon substrate around the tuning region by performing dry-etching processes in steps (v) and (vi), forming air trenches. [27] The cross sectional view of the fabricated device, shown in Fig. 3(c), indicates that the substrate was successfully removed.

We first characterized the SHG by launching a telecom-band tunable laser into a pumping device. We used a fiber polarization controller (FPC) and two tapered fibers to couple the TE_{00} mode. We adopted a cladded double-layer inversed-taper LN mode size converter [28] in the input port for efficient coupling of FW light. The measured fiber-to-chip coupling losses were 2.2 dB/facet at FW and 5 dB/facet at SH, respectively. By scanning the pump

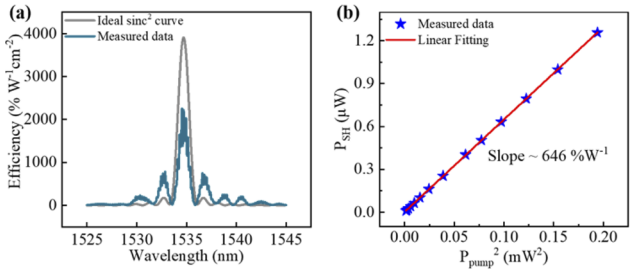

Fig. 4. (a) SHG conversion spectrum of device with poling period of 2.9 μm. (b) Second harmonic power as a function of pump power with fixed wavelength of 1535.7 nm. Linear fitting of the experimental data exhibits an on-chip conversion efficiency of 646% W^{-1}.

wavelength, we recorded the conversion efficiency spectrum of SHG and measured the $sinc^2$-like curve plotted in Fig. 4(a) (blue line). The main peak was located at 1535.7 nm with a full width at half maximum of 1 nm. Compared with the theoretical expectation [gray line in Fig. 4(a)], the measured side peaks likely were introduced by the potential non-uniformity of the waveguide thickness along its propagation direction, which is also the primary reason for the reduction in the main peak efficiency [29,30]. By varying the power of the fundamental light with a fixed wavelength of 1535.7 nm, we recorded the power-dependent SH response by using a silicon power meter. In Fig. 4(b), SH shows a quadratic power dependence on FW, which agrees well with the theoretical expectation. By using the fitted slope of 646% W^{-1}, we calculated the on-chip normalized efficiency to be 2580% W^{-1} cm^{-2}, ~61% of the theoretical efficiency of 4200% W^{-1} cm^{-2}.

Figure 5(a) shows the experimental setup for the thermal tunability and dynamic time response. We first used a voltage source and DC probes to apply DC voltages to the heater. We calculated the heating powers as the product of the applied voltages and currents. Figure 5(b) shows the SHG conversion profiles measured at 0, 15, 26, 40, and 50 mW. The QPM wavelength can be continuously tuned from 1534.8 to 1539.6 nm with an efficiency variation of <500% W^{-1} cm^{-2}. We achieved the highest SHG conversion efficiency at 3000% W^{-1} cm^{-2} by heating at 40 mW. By mapping the QPM wavelength as a function of heating power, we obtained a large tuning slope of 94 pm/mW [see Fig. 5(c)]. A smaller slope than the simulated one is possible because of other thermally induced nonlinear effects, such as the thermal expansion effect [31,32]. Then, we investigated the dynamic time response of the devices by launching a square-wave electrical signal via an arbitrary waveform generator (AWG). The frequency, amplitude, and duty cycle of the electrical signal were 100 Hz, 4 V, and 50%, respectively. We detected the output SH light intensity by using a Si PD and then recorded it by an oscilloscope together with the trigger signal. Initially, we fixed the pumping wavelength at the QPM wavelength. With a 4-V heating signal, the SH signal was attenuated due to the phase mismatch [see Fig. 5(d)]. Compared with the electrical signal, the waveforms of the light signal have slightly smoother edges indicating the slow response of the heat generation and dissipation. The heating and cooling time were measured to be 0.5 and 1 ms, respectively, corresponding to a TO bandwidth of 700 Hz.

To conclude, benefiting from the design of an integrated microheater with a thermally isolated structure, we demonstrate

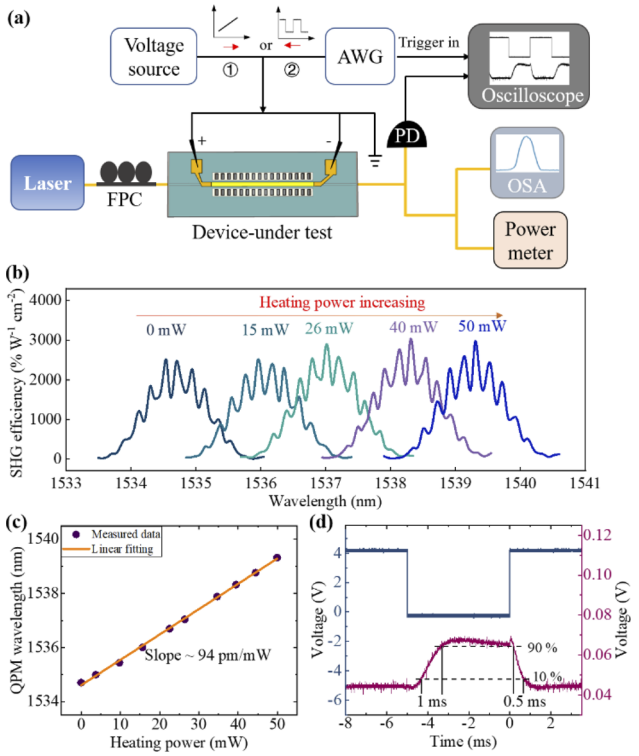

Fig. 5. (a) Experimental setup for thermal tuning of SHG and thermal response time: fiber polarization controller (FPC), photodetector (PD), arbitrary waveform generator (AWG), and optical spectrum analyzer (OSA). (b) Conversion efficiency spectra at different heating power. (c) Measured phase-matched FW as a function of heating power. (d) Time response of the device. Blue curve is the waveforms of the input electric signal; red curve is the output optical power signal.

a highly tunable SHG process while sustaining high conversion efficiency with a type-0 QPM scheme. This allowed us to achieve a high thermal-tuning efficiency of 94 pm/mW. Meanwhile, the phase-matching profiles maintained a high peak conversion efficiency of 2500–3000% $W^{-1}\,cm^{-2}$ with an average bandwidth of 1 nm over the entire tuning range. Our device shows great promise for efficient on-chip wavelength conversion to produce highly tunable miniature coherent visible light for broad applications, while taking advantage of mature and cost-effective telecom laser technology.

Funding. National Key Research and Development Program of China (2019YFA0705000, 2019YFB1803900); Local Innovative and Research Teams Project of Guangdong Pearl River Talents Program (2017BT01X121); Key R&D Program of Guangdong Province (2018B030329001); National Natural Science Foundation of China (11761131001).

Disclosures. The authors declare no conflicts of interest.

Data availability. No data were generated or analyzed in the presented research.

REFERENCES

1. R. W. Boyd, *Nonlinear Optics* (Academic, 2003).
2. G.-T. Xue, Y.-F. Niu, X. Liu, J.-C. Duan, W. Chen, Y. Pan, K. Jia, X. Wang, H.-Y. Liu, Y. Zhang, P. Xu, G. Zhao, X. Cai, Y.-X. Gong, X. Hu, Z. Xie, and S. Zhu, Phys. Rev. Appl. **15**, 064059 (2021).
3. X. Lu, Q. Li, D. A. Westly, G. Moille, A. Singh, V. Anant, and K. Srinivasan, Nat. Phys. **15**, 373 (2019).
4. K. A. Fedorova, G. S. Sokolovskii, M. Khomylev, D. A. Livshits, and E. U. Rafailov, Opt. Lett. **39**, 6672 (2014).
5. Y. M. Sua, J.-Y. Chen, and Y.-P. Huang, Opt. Lett. **43**, 2965 (2018).
6. T. Kobayashi, S. Shimizu, M. Nakamura, T. Umeki, T. Kazama, R. Kasahara, F. Hamaoka, M. Nagatani, H. Yamazaki, H. Nosaka, and Y. Miyamoto, J. Lightwave Technol. **39**, 787 (2021).
7. M. Jankowski, N. Jornod, C. Langrock, B. Desiatov, A. Marandi, M. Lončar, and M. M. Fejer, Optica **9**, 273 (2022).
8. G. P. Agrawal, *Fiber-Optic Communication Systems* (Wiley, 2012).
9. M.-G. Suh, Q.-F. Yang, K. Y. Yang, X. Yi, and K. J. Vahala, Science **354**, 600 (2016).
10. T. Udem, R. Holzwarth, and T. W. Hänsch, Nature **416**, 233 (2002).
11. F. Vollmer and S. Arnold, Nat. Methods **5**, 591 (2008).
12. R. S. Weis and T. K. Gaylord, Appl. Phys. A **37**, 191 (1985).
13. V. Gopalan, V. Dierolf, and D. A. Scrymgeour, Annu. Rev. Mater. Res. **37**, 449 (2007).
14. G. Poberaj, H. Hu, W. Sohler, and P. Günter, Laser Photonics Rev. **6**, 488 (2012).
15. Y. Niu, C. Lin, X. Liu, Y. Chen, X. Hu, Y. Zhang, X. Cai, Y.-X. Gong, Z. Xie, and S. Zhu, Appl. Phys. Lett. **116**, 101104 (2020).
16. A. Rao, K. Abdelsalam, T. Sjaardema, A. Honardoost, G. F. Camacho-Gonzalez, and S. Fathpour, Opt. Express **27**, 25920 (2019).
17. C. Wang, C. Langrock, A. Marandi, M. Jankowski, M. Zhang, B. Desiatov, M. M. Fejer, and M. Lončar, Optica **5**, 1438 (2018).
18. J. Zhao, M. Rüsing, U. A. Javid, J. Ling, M. Li, Q. Lin, and S. Mookherjea, Opt. Express **28**, 19669 (2020).
19. X. Liu, S. Gao, C. Zhang, Y. Pan, R. Ma, X. Zhang, L. Liu, Z. Xie, S. Zhu, S. Yu, and X. Cai, Adv. Photon. Nexus **1**, 016001 (2022).
20. J. Chen, "Nonlinear and Quantum Photonics in Thin-Film Lithium Niobate," Ph.D. dissertation (Stevens Institute of Technology, 2020).
21. R. Luo, Y. He, H. Liang, M. Li, and Q. Lin, Optica **5**, 1006 (2018).
22. C. Lu, Y. Zhang, J. Qiu, Y. Tang, T. Ding, S. Liu, Y. Zheng, and X. Chen, Opt. Lett. **47**, 1081 (2022).
23. J.-Y. Chen, C. Tang, Z.-H. Ma, Z. Li, Y. M. Sua, and Y.-P. Huang, Opt. Lett. **45**, 3789 (2020).
24. G. Yi, W. Liang, and C.-Q. Xu, Proc. SPIE **6875**, 687506 (2008).
25. L. Moretti, M. Iodice, F. G. Della Corte, and I. Rendina, J. Appl. Phys. **98**, 036101 (2005).
26. M. M. Fejer, G. A. Magel, D. H. Jundt, and R. L. Byer, IEEE J. Quantum Electron. **28**, 2631 (1992).
27. X. Liu, Y. Pan, X. Zhong, J. Xu, Y. Han, S. Yu, and X. Cai, Opt. Lett. **45**, 6318 (2020).
28. L. He, M. Zhang, A. Shams-Ansari, R. Zhu, C. Wang, and L. Marko, Opt. Lett. **44**, 2314 (2019).
29. M. Santandrea, M. Stefszky, G. Roeland, and C. Silberhorn, New J. Phys. **21**, 123005 (2019).
30. X.-H. Tian, W. Zhou, K.-Q. Ren, C. Zhang, X. Liu, G.-T. Xue, J.-C. Duan, X. Cai, X. Hu, Y.-X. Gong, Z. Xie, and S.-N. Zhu, Chin. Opt. Lett. **19**, 060015 (2021).
31. D. H. Jundt, Opt. Lett. **22**, 1553 (1997).
32. Y. Kim and R. Smith, J. Appl. Phys. (Melville, NY, U. S.) **40**, 4637 (1969).